

Electronic structure and magnetism in two-dimensional hexagonal $5d$ transition metal carbides, $\text{Ta}_{n+1}\text{C}_n$ ($n = 1, 2, 3$)

Nina J. Lane,¹ Michel W. Barsoum,¹ and James M. Rondinelli¹

Department of Materials Science & Engineering, Drexel University, Philadelphia, PA 19104, USA

Density functional calculations are used to investigate the electronic structure of two-dimensional $5d$ tantalum carbides with honeycomb-like lattice structures. We focus on changes in the low-energy bands near the Fermi level in pristine sheets of $\text{Ta}_{n+1}\text{C}_n$ with increasing dimensionality (n). We find that the Ta $5d$ states dominate, but due to the extended nature of the wavefunctions, they are weakly correlated. The carbide sheets are prone to long range magnetic order, and we evaluate the stability of these states to enhanced electron–electron interactions, which we include using an onsite Hubbard U correction. Lastly, we find spin orbit interactions strongly renormalize the band structure for $n = 2$, but play a minor role in $n = 1$ and 3 sheets.

Two-dimensional (2D) free-standing crystals exhibit a range of functional properties, mainly derived from the topology of their underlying lattice and enhanced electronic and magnetic effects due to reduced dimensionality. Spin-polarized edge states,¹ for example, have been predicted for the well-studied 2D carbon material graphene,² owing to the topological origin of its transport properties. A large external magnetic field, however, is required to realize the quantum Hall effect, and its spin degeneracy makes it difficult to manipulate. To overcome these challenges, experimental approaches have been developed to induce magnetism by introducing transition metal adatoms³ and point defects⁴ on the surfaces.

2D binary metal oxides and dichalcogenides, e.g. ZnO , BN , MoS_2 also find widespread interest. New functionalities originate from the presence of more diverse chemistries.^{5,6} However, in most existing pristine 2D free standing materials, magnetic ordering is absent and the tunability of the electronic structure is limited to electrostatic doping. A more promising avenue includes directly incorporating transition metals with multiple orbital degrees of freedom and highly-correlated electrons into to the lattice. Magnetism, for example, was recently predicted for VX_2 ($X=\text{S, Se}$) monolayers.⁷ Alternatively, heavier $5d$ transition metals with strong spin orbit coupling can be either deposited on the surface or directly integrated into the lattice of the 2D materials. Recent first principles calculations show that graphene decorated with $5d$ transition metals can exhibit remarkable magnetic and topological transport properties.⁸ The magnetic coupling induced by such treatments on nonmagnetic 2D materials, however, is difficult to control in actual applications due to unintentional impurities and defects.

In this Letter, we focus on novel low-dimensional hexagonal materials, consisting of alternating layers of carbon and tantalum. These Ta-containing transition metal carbides are part of a new group of 2D materials called “MXenes,” recently synthesized by chemical exfoliation.⁹ Similar to the previously studied Ta-decorated graphene structures,⁸ these materials contain sheets of carbon in the inner layers and Ta atoms on the surface. In this case, however, the Ta layers are ordered, rendering them less susceptible to defects and more favorable for deliberate

surface functionalization. Furthermore, these materials are derived from MAX phases, which are a large family of layered carbides and nitrides with the general formula $M_{n+1}AX_n$, where $n = 1 \cdots 3$, M is an early transition metal, A is an A-group element (mostly from groups 13 and 14), and X is carbon and/or nitrogen.¹⁰ Since the stacking sequence of the XM_6 octahedra in the hexagonal MAX phases depends on the stoichiometry, the MXene sheets have the advantage that dimensionality controls both the system size and the symmetry between the two surfaces (Fig. 1a).

The 2D MXenes have the general formula $M_{n+1}X_n$, and they crystallize in sheets containing 1, 2, or 3 layers of XM_6 octahedra depending on n . Their recent synthesis⁹ has led to a number of theoretical studies,^{11–13} mainly focusing on the Ti-containing phases. However, MXenes in the Ta-C system have not yet been well studied.

Motivated by the structural flexibility, possible enhanced electron–electron interactions, and the strong spin-orbit coupling parameter for Ta ($\zeta_d = 1970 \text{ cm}^{-1}$),¹⁴ we use *ab initio* electronic structure calculations to investigate the effect of dimensionality (n) and electron correlations on the band structure and magnetic ordering in $\text{Ta}_{n+1}\text{C}_n$, $n = 1 \cdots 3$.

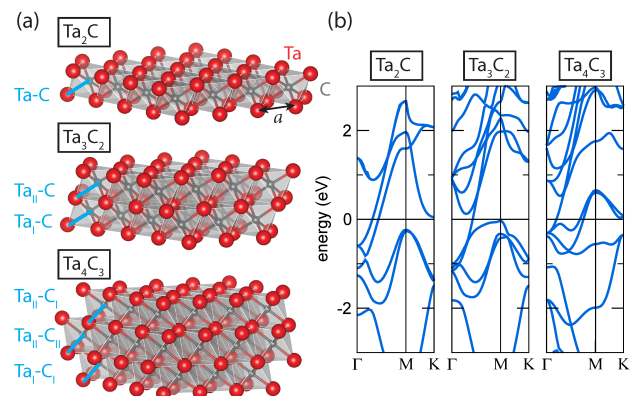


FIG. 1. The two-dimensional $\text{Ta}_{n+1}\text{C}_n$ ($n = 1, 2, 3$) sheets (a) all possess hexagonal symmetry. The lattice constants, a , and select interatomic Ta–C distances are highlighted (cf. Table I). (b) LDA electronic band structures for each compound along the path $\Gamma(0, 0, 0) \rightarrow M(\frac{1}{2}, 0, 0) \rightarrow K(\frac{1}{2}, \frac{1}{2}, 0)$.

TABLE I. Summary of lattice parameters, a , and Ta–C bond lengths, d , in Å with respect to dimensionality, n , obtained with LDA and PBEsol functionals. Embolden values correspond to experimental data taken from Ref. 19.

	n	length	LDA	PBEsol
Ta ₂ C	1	a	3.041	3.058
		$d(\text{Ta–C})$	2.127	2.139
Ta ₃ C ₂	2	a	3.086	3.112
		$d(\text{Ta}_\text{I}–\text{C})$	2.110	2.127
		$d(\text{Ta}_\text{II}–\text{C})$	2.220	2.236
Ta ₄ C ₃	3	a	3.077	3.094
		$d(\text{Ta}_\text{I}–\text{C})$	2.119	2.131
		$d(\text{Ta}_\text{II}–\text{C})$	2.201	2.210
		$d(\text{Ta}_\text{II}–\text{C}_\text{II})$	2.215	2.226

First-principles density functional calculations are performed using the Vienna *Ab initio* Simulation Package (VASP),¹⁵ with a plane wave cutoff of 500 eV and the projector-augmented wave method (PAW)¹⁶ to treat the interaction between the core and valence electrons; we treat the Ta 5*p* electrons as valence electrons. Reciprocal space integrations are performed using a $9 \times 9 \times 2$ k -point mesh. We investigate the effects of electron–electron interactions by using both the local (spin) density approximation [L(S)DA] and the improved generalized gradient approximation (GGA) of Perdew–Burke–Erzerhof (PBEsol) for solids¹⁷ with the rotationally invariant Hubbard U correction (+ U) of Liechtenstein *et al.*,¹⁸ keeping $J = 0.5$ eV throughout. The high measured conductivity of Ta₄C₃,¹⁹ and the robustly metallic electronic structures of bulk TaC²⁰ and the MAX phases,¹⁰ suggest that any electron correlation effects should be weak. We, therefore, anticipate the LDA and PBEsol functionals to provide an adequate description of the electronic and magnetic properties of these materials.

The Ta _{$n+1$} C _{n} unit cells used in our calculations contain two symmetry equivalent free-standing sheets that are separated by 11–13 Å of vacuum. We obtained the equilibrium structures at the LDA and PBEsol level by minimization of the total energy computed for a range of a lattice parameters, performing a full relaxation of the atomic positions along the c -direction until the forces were converged below a tolerance of 5 meV Å^{−1}.

Table I contains the ground state atomic structure descriptors obtained with the LDA and PBEsol functionals. The LDA functional, for all values of n , predicts equilibrium lattice parameters that are smaller than those obtained with PBEsol; nonetheless, both functionals are in good agreement, within < 1% of each other and the available experimental data¹⁹ for Ta₄C₃. We also summarize the interatomic distances between the different Ta and C atoms corresponding to the sites labeled in Fig. 1(a). For all 2D sheets explored, the Ta atoms at the surface layer have shorter Ta–C bonds than those in the center of the sheet, i.e. $d(\text{Ta}_\text{I}–\text{C}) < d(\text{Ta}_\text{II}–\text{C})$.

While there are slight differences in the lattice dimen-

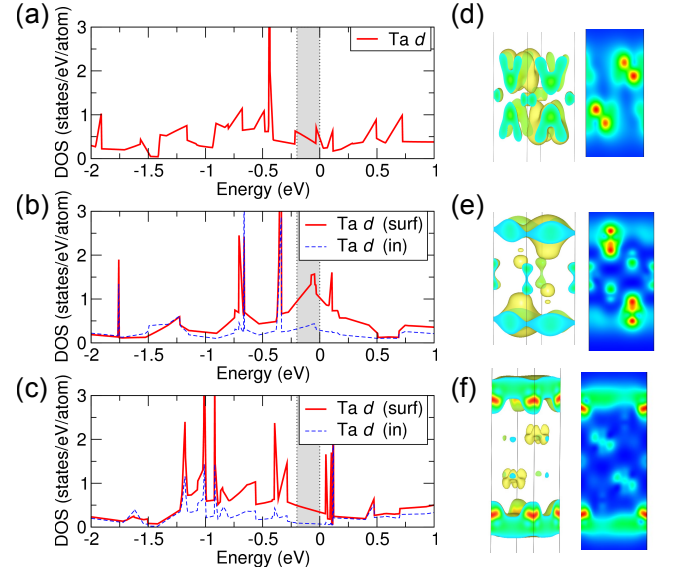


FIG. 2. Site-decomposed partial DOS computed within the LDA for the surface (surf) and inner (in) layer Ta sites in (a) Ta₂C, (b) Ta₃C₂, and (c) Ta₄C₃. Note that the contribution from the C atoms to the DOS within this energy window is small and therefore not shown. The spatial distribution of the partial charge density from 0.2 eV up to the Fermi level (shaded region) is also shown in (d), (e), and (f) for Ta₂C, Ta₃C₂, and Ta₄C₃, respectively. The 2D contours are projections on the (11 $\bar{2}$ 0) plane.

sions and atomic positions, the average interatomic distances and lattice parameters are similar between the three stoichiometries. This suggests that any differences in electronic structure should originate from either the stacking of the octahedra or the number of occupied Ta d bands available, which depends on the ratio of Ta to C atoms. To explore these possible differences, we begin by computing the electronic band structures with the LDA functional. For $n = 1$, we find two dispersive Ta d -bands crossing the Fermi level (E_F) along $\Gamma - \text{M}$ [Fig. 1(b), left]. Other than the points near Γ where these two bands cross E_F , the Fermi level falls in the band gap present along most of the sampled path in the Brillouin zone (BZ). These two free-electron pockets centered at Γ are similar to those found in 3D metals despite the 2D nature of the MXene sheet. In contrast, we find in Ta₃C₂ ($n = 2$) a single Ta band that crosses the Fermi level along $\Gamma - \text{M}$ with nearly linear dispersion [Fig. 1(b), center]. Due to the symmetry of the BZ, there is another linear band crossing of this type along $\text{K} - \Gamma$. At the M-point, the band just below E_F , corresponding to a Ta d orbital, is fully occupied. The band structure for Ta₄C₃ ($n = 3$), on the other hand, is strongly metallic; three Ta d bands cross E_F [Fig. 1(b), right]. The lower two bands rise above E_F around the M-point and again cross the Fermi level at the K-point. Indeed the site-decomposed partial densities-of-states (DOS) confirm that the region near E_F is largely controlled by the Ta d states [Figs. 2(a–c)].

Figs. 2(d–f) show the spatial distribution of the electrons within 0.2 eV of E_F . We find a strong dependence

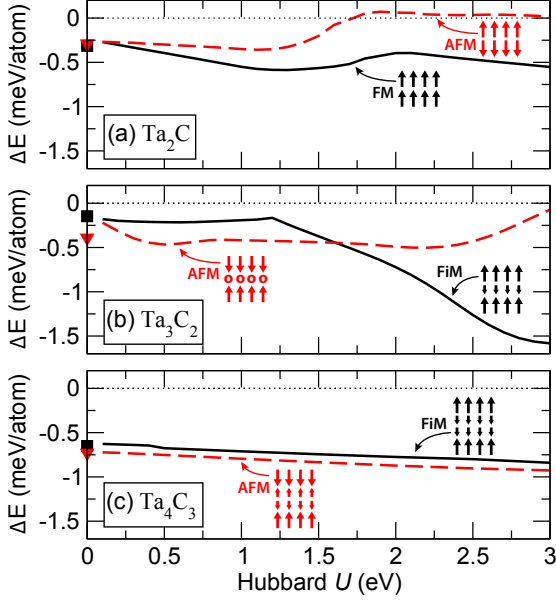


FIG. 3. The L(S)DA+ U energy differences, ΔE , between the magnetic and non-spin polarized (NSP) states with U for (a) Ta_2C , (b) Ta_3C_2 , and (c) Ta_4C_3 . Energies given per Ta atom. The points at $U = 0$ eV are obtained without the plus Hubbard U method. Schematics (inset) illustrate the spin ordering of the Ta atoms with ferromagnetic (FM), ferrimagnetic (FiM), or antiferromagnetic (AFM) order; the arrows represent the relative magnitudes and directions of spin, and the open circles indicate a Ta atom with no magnetic moment.

on dimensionality for the charge distribution. Intriguingly, this spatial distribution about the Ta site in $n = 1$, *viz* Ta_2C [Fig. 2(d)], and the inner Ta atom in $n = 3$, *viz* Ta_4C_3 [Fig. 2(f)], share similar features—the charge around the atom is distributed into six lobes, three above and three below the Ta atom. The inner Ta atom in $n = 2$ (Ta_3C_2) [Fig. 2(d)] shows strikingly different behavior, with a small distribution of charge collected above and below the Ta atom, aligned parallel to the c -axis.

To understand the atomic-scale origin of these features, we examine more closely the crystal structures of each sheet. Ta_2C ($n = 1$) consists of a single Ta–C octahedron with stacking sequence AcB, where uppercase letters denote the Ta atom and lower case letters represent the stacking of carbon atoms. Ta_4C_3 ($n = 3$), therefore, is obtained as a Ta_2C layer, AcB, with an extra Ta atom on each surface – that is, Cb[AcB]aC. Note that this is the only structure in which two Ta atoms on either surface have the same stacking. On the other hand, Ta_3C_2 ($n = 2$) has a stacking sequence of AcBaC, so the symmetry of the AcB layer is broken due to the odd number of layers. This suggests that the differences in the charge distribution we find in Figs. 2(d–f) are largely governed by the stacking sequence of the CTa_6 units—a degree of freedom unique to the MXene phases. Such differences in the electron distribution near E_F due to the asymmetric stacking are also visible in the shape of the DOS [shaded region in Fig. 2(b)]. The charge is concentrated at the surface for Ta_3C_2

TABLE II. Summary of the stable spin polarized ground states for the $\text{Ta}_{n+1}\text{C}_n$ MXene phases using different exchange-correlation functionals with and without a Hubbard U correction. Notations (schematics) for the magnetic states are given in the caption (insets) to Fig. 3.

	Ta_2C	Ta_3C_2	Ta_4C_3
LDA	FM	AFM	AFM
LDA+ U	FM ($U > 0$)	FM ($U > 1.6$)	AFM
PBEsol	AFM	AFM	NSP
PBEsol+ U	FM ($U > 0.1$)	FM ($U > 0.9$)	NSP

and Ta_4C_3 , consistent with the higher partial density of states for the Ta surface atoms [Figs. 2(b–c)].

The large number of Ta d -states at E_F and the sensitivity of the electronic structure to the sheet dimensionality suggest the possibility of stable long range magnetic spin configurations. We therefore performed a series of spin-polarized calculations with two different starting configurations, corresponding to ferromagnetic (FM) and antiferromagnetic (AFM) spin order on the Ta sites, to systematically explore the possible magnetic orders with respect to n . We carried out unconstrained-spin density calculations to find the stable magnetic ordering (Fig. 3) and compared the total energy of those states to that of the non-spin-polarized case. Given the limited ability of DFT to fully capture correlation effects, including transition metal ions with partially filled d shells, we now add the Hubbard U correction to the standard PBEsol (PBEsol+ U) and LSDA (LSDA+ U) functionals.²¹ Since it was recently suggested that Ta-containing MAX phases are weakly correlated,²² we explored $U < 3.0$ eV.

Figure 3 shows the change in total energy computed with the LSDA+ U functional compared to the non-spin-polarized (NSP) case as a function of U . In all cases, the magnetically ordered configurations are lower in energy than the NSP state. As the dimensionality increases, the AFM case becomes more stable, likely due to the fact that the Ta atoms on each surface are more strongly spin-polarized. Our main results are summarized in Table II, where the values in parentheses specify the U values above which the specific magnetic ordering becomes stable. For Ta_2C and Ta_3C_2 , both LSDA+ U and PBEsol+ U calculations predict a FM configuration, whereas an AFM ordering is predicted for Ta_4C_3 , but only with the LSDA+ U exchange-correlation functional (Table II). Note that in Ta_4C_3 no magnetic configurations were found to be stable using either PBEsol and PBEsol+ U .

In general, a larger Hubbard U value leads to a more stable ferromagnetic (or ferrimagnetic) configuration, especially for Ta_3C_2 [Fig. 3(b)]. In all cases, the surface Ta atoms are spin polarized in the same direction for FM and FiM order and in opposite directions for AFM. The Ta atoms in the inner layers are weakly spin-polarized in the direction opposite to the surface Ta atoms in both the FiM and AFM configurations, with the exception of the AFM configuration of Ta_3C_2 , which is constrained by

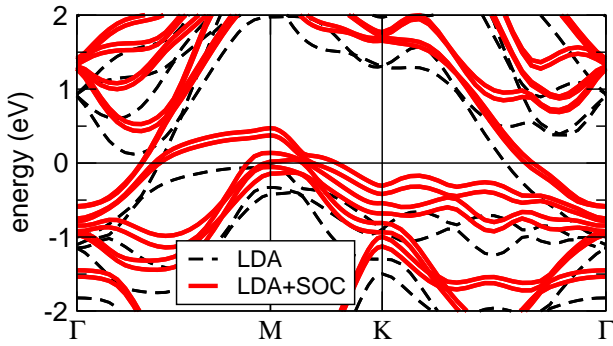


FIG. 4. LDA band structure for Ta_3C_2 without (black, broken lines) and with (red, solid lines) spin-orbit coupling (SOC).

symmetry. The addition of U generally has a small effect on the electronic structure, leading to a slight shift of the Ta d -bands uniformly to higher energies. In Ta_3C_2 , whose band structure is controlled largely by a single band that is partially filled, the addition of correlation effects drives a transition from a state with a single band crossing E_F to a multi-band metal with a complex Fermi surface.

Having established that the long-range magnetic order due to the spin exchange splitting of the Ta d states at E_F strongly alters the orbital filling, we now evaluate the effect of spin-orbit coupling (SOC) on the band structure with respect to n . Here we find that SOC splits the band, manifesting as a shift of the Ta d -bands to higher energy levels in all cases; it has the strongest effect on Ta_3C_2 (Fig. 4), where the band structure changes from a nearly single band at the Fermi level to one with multiple band crossings throughout the Brillouin zone. The addition of SOC destroys the single band crossing in manner similar to that found for a finite U value. The spin-orbit splitting at the top of the valence band ($\Delta_{SO}=148$ meV) is approximately half of that observed in GaAs ($\Delta_{SO}=342$ meV),²³ but more than 3 orders of magnitude larger than graphene ($\Delta_{SO} \approx 0.05$ meV).²⁴ The result is that a single band n -type metal with linear dispersion transforms into a multi-band p -type conductor with hole pockets, which should exhibit a strongly temperature dependent thermopower.

In summary, we have shown that the Ta-based 5d electronic structure is highly sensitive to dimensionality. All explored phases exhibit correlation stabilized magnetic order that is not found in the bulk MAX phase structures. The LSDA+ U method stabilizes the ferromagnetic ordering in the case of $n = 1, 2$, and for $n = 2$ spin-orbit coupling renormalizes the electronic band structure with a transition from a nearly filled single band to a metal. In these 2D MXenes, the electronic structure is controlled by the stacking of the XTa_6 octahedra and the states derived from the surface Ta atoms. Tailoring the electronic structure could therefore be achieved through end group functionalization of the surfaces of the MXene sheets. This opens up possibilities for engineering a new class of tunable functional 2D materials. We conjecture that one could maintain a graphene-like band structure

like that observed in Ta_3C_2 by through epitaxial strain engineering. Overall, the Ta-containing graphene-like carbides show great promise as functional 2D materials that can be synthesized in different dimensionalities, leading to a range of stacking sequences and stoichiometries that offer a variety of electronic and magnetic behaviors.

ACKNOWLEDGMENTS

N.J.L. and M.W.B. were supported by the Assistant Secretary for Energy Efficiency and Renewable Energy, Office of Vehicle Technologies of the U.S. DOE under Contract No. DE-AC02-05CH11231, Subcontract 6951370 under the Batteries for Advanced Transportation Technologies (BATT) Program. N.J.L. acknowledges financial support by the Integrated Graduate Education and Research Traineeship (IGERT) under NSF (DGE-0654313), and J.M.R. was supported by ARO (W911NF-12-1-0133). This work benefited from the XSEDE (NSF) and the Center for Nanoscale Materials (U.S. DOE-BES, under Contract No. DE-AC02-06CH11357) HPC resources.

- ¹C. L. Kane and E. J. Mele, Phys. Rev. Lett. **95**, 226801 (2005).
- ²K. S. Novoselov, A. K. Geim, S. V. Morozov, D. Jiang, D. Zhang, S. V. Dubonos, I. V. Grigorieva, and A. A. Firsov, Science **306**, 666 (2004).
- ³A. V. Krasheninnikov, P. O. Lehtinen, A. S. Foster, P. Pyykko, and R. M. Nieminen, Phys. Rev. Lett. **102**, 126807 (2009).
- ⁴J. S. Crvenka, M. I. Katsnelson, and C. F. J. Flipse, Nat. Phys. **5**, 840 (2009).
- ⁵A. M. Seayad and D. M. Antonelli, Adv. Mater. **16**, 765 (2004).
- ⁶Y. D. Ma, Y. Dai, W. Wei, C. N. Niu, L. Yu, and B. B. Huang, J. Phys. Chem. C **115**, 20237 (2011).
- ⁷Y. Ma, Y. Dai, M. Guo, C. Niu, Y. Zhu, and B. Huang, ACS Nano **6**, 1695 (2012).
- ⁸H. Zhang, C. Lazo, S. Blügel, S. Heinze, and Y. Mokrousov, Phys. Rev. Lett. **108**, 056802 (2012).
- ⁹M. Naguib, M. Kurtoglu, V. Presser, J. Lu, J. Niu, M. Heon, L. Hultman, Y. Gogotsi, and M. W. Barsoum, Adv. Mater. **23**, 4207 (2011).
- ¹⁰M. W. Barsoum, Prog. Sol. Stat. Chem. **28**, 201 (2000).
- ¹¹Q. Tang, Z. Zhou, P. Shen, J. Am. Chem. Soc. (2012) *In print*.
- ¹²I. R. Shein, A. L. Ivanovskii, Superlattice Microst. **52**, 147-157 (2012).
- ¹³M. Kurtoglu, M. Naguib, Y. Gogotsi, M. W. Barsoum, MRS Comm. (2012) *In print*.
- ¹⁴M. Montalti, A. Credi, L. Prodi, and M. T. Gandolfi, *Handbook of Photochemistry* (CRC Press, 2006).
- ¹⁵G. Kresse and J. Furthmüller, Phys. Rev. B **54**, 11169 (1996).
- ¹⁶P. E. Blöchl, Phys. Rev. B **50**, 17953 (1994).
- ¹⁷J. P. Perdew, A. Ruzsinszky, G. I. Csonka, O. A. Vydrov, G. E. Scuseria, L. A. Constantin, X. Zhou, and K. Burke, Phys. Rev. Lett. **100**, 136406 (2008).
- ¹⁸A. I. Liechtenstein, V. I. Anisimov, and J. Zaanen, Phys. Rev. B **52**, R5467 (1995).
- ¹⁹M. Naguib, O. Mashtalir, J. Carle, V. Presser, J. Lu, L. Hultman, Y. Gogotsi, and M. W. Barsoum, ACS Nano **6**, 1322 (2012).
- ²⁰H. Li, L. Zhang, Q. Zeng, K. Guan, K. Li, H. Ren, S. Liu, and L. Cheng, Sol. Stat. Comm. **151**, 602 (2011).
- ²¹V. I. Anisimov, A. I. Poteryaev, M. A. Korotin, A. O. Anokhin, and G. Kotliar, J. Phys.: Condens. Matter **9**, 7359 (1997).
- ²²W. Sun, W. Luo, and R. Ahuja, Journal of Materials Science **47**, 7615 (2012).
- ²³P. Carrier and S.-H. Wei, Phys. Rev. B **70**, 035212 (2004).
- ²⁴J. C. Boettger and S. B. Trickey, Phys. Rev. B **75**, 121402 (2007).